

Influence of particle shape and material on the acoustic radiation force and microstreaming in a standing wave

Alen Pavlic ^{*}, Pushkin Nagpure , Lorenzo Ermanni , and Jürg Dual
Institute for Mechanical Systems, ETH Zurich, 8092 Zurich, Switzerland

 (Received 12 March 2022; accepted 16 June 2022; published 13 July 2022)

In view of its influence on the acoustic radiation force, we investigate the microstreaming around a small solid elastic particle in an ultrasonic standing wave in dependence of its material properties and shape. The configuration is axisymmetric, making it accessible to numerical methods, such as the finite element method. The results reveal a transition from viscous scattering- to microstreaming-dominated acoustic radiation force that depends on the particle density. When a deviation of the particle shape from a sphere becomes smaller than the viscous boundary layer thickness, we show that the influence of the shape on the viscous contributions to the acoustic radiation force diminishes, allowing the use of theoretical models for a spherical particle. However, extreme asymmetric shape perturbations, such as crowns with sharp edges, can give rise to noticeable viscous contributions for a dense particle that is larger than the viscous boundary layer thickness. We also introduce a hybrid analytical model for the acoustic radiation force on a spherical particle that accounts for the microstreaming and particle compressibility and shows a good agreement with numerical simulations for an arbitrary particle size and density.

DOI: [10.1103/PhysRevE.106.015105](https://doi.org/10.1103/PhysRevE.106.015105)

I. INTRODUCTION

Man-made and natural μm -sized particles consisting of various materials often deviate from a spherical shape, such as amoeba with pseudopods [1], bacteria of cylindrical shape [2], nano-urchins with spikes [3], or the red blood cells with their cross section resembling the Cassinian oval [4], to name a few. Acoustophoresis — particle motion induced by acoustic waves — can be used, for example, to separate [5], trap [6], and focus [7] such particles. However, most theories on the acoustic forces assume a spherical particle shape, while some account for the irregular particle shape, but only with the assumption of an inviscid fluid [8–15]. This leads to an unknown influence of particle shape on acoustic forces for small particle sizes, at which viscosity plays an important role.

When a single spherical particle with radius a is considered, the main forces on the particle in an acoustic field are the acoustic radiation force (ARF) and the Stokes drag from the acoustic streaming [16], scaling with a^3 and a , respectively. The steady acoustic streaming generally originates from the interaction of acoustic waves with boundaries (Rayleigh [17] and Schlichting [18] streaming) or from the wave attenuation in the fluid bulk (Eckart [19] streaming). Meanwhile, the ARF results from the interaction between the wave scattered at the particle and the background wave, which is often a plane standing wave [20]; this interaction also produces the steady microstreaming around the particle [21] that influences the ARF [22] and is superimposed to the environmental (Rayleigh or Eckart) streaming [23].

The aforementioned scaling of the ARF and the Stokes drag from the environmental streaming limits the acoustic manipulation to $a \approx 1.34 \mu\text{m}$ for polystyrene particles in water at the frequency $f = 500 \text{ kHz}$ [24]. In recent years, however, great efforts have been made to suppress the acoustic streaming inside systems for acoustic manipulation of μm -sized particles and cells [25–30]. These methods might enable manipulation of particles that are small compared to the viscous boundary layer thickness $\delta = \sqrt{\eta/(\rho_0 \pi f)}$, which is $\approx 0.74 \mu\text{m}$, for $f = 500 \text{ kHz}$ in water, with dynamic viscosity $\eta = 1 \text{ mPa s}$ and equilibrium density $\rho_0 = 1000 \text{ kg m}^{-3}$.

Since King's model [31] of the ARF on a rigid sphere in an inviscid fluid, in 1934, the theoretical models of the ARF have been gradually expanded [22,32–38]. In his formulation of the ARF, Doinikov [22] eliminated the assumption on the inviscid fluid, accounting for the microstreaming around a rigid particle and for the viscous scattering effects. The theory was further validated by a finite-element method (FEM) analysis [39], confirming Doinikov's prediction that the microstreaming can shift the equilibrium position of a heavy particle, from a pressure node to an antinode of a standing wave. Furthermore, Rednikov and Sadhal have studied the microstreaming around rigid objects extensively, using analytical methods [40,41]. Their analysis is, however, limited to $a \gg \delta$ and does not extend to the ARF.

The influence of viscous scattering and of microstreaming is understood to increase with the density contrast between the particle and the fluid, and with the decreasing particle size [39,42]. However, the theory behind the ARF in the $a \lesssim \delta$ regime needs to be further explored, in order to understand how the particle shape and the particle material influence the viscous scattering and microstreaming contributions to the total ARF.

^{*}apavlic@ethz.ch

Here we use a previously validated numerical model [39] to investigate the influence of the shape and material on the ARF for particles that are comparable or smaller than the viscous boundary layer thickness δ , and smaller than the acoustic wavelength in a standing wave (Rayleigh limit). We decompose the total ARF into four parts: (1) the inviscid force on an equivalent compressible sphere F_{yos} that follows from Yosioka and Kawasima [32], (2) the inviscid scattering contribution due to shape deviation \tilde{F}_{scat} , (3) the viscous scattering contribution \tilde{F}_{vsc} , and finally (4) the microstreaming contribution \tilde{F}_{str} . We show that for different particle materials, spanning from polystyrene to gold in water, the viscous contributions for $\delta/a > 1$ are generally dominated by \tilde{F}_{str} , even though \tilde{F}_{str} and \tilde{F}_{vsc} are both increasing with the particle density at $\delta/a > 1$. At $\delta/a \gg 1$, the total ARF is dominated by \tilde{F}_{str} , except for the nearly neutrally buoyant particles (e.g., polystyrene in water). When the viscous effects start to rise, at $\delta/a \approx 1$, we find that \tilde{F}_{vsc} can be greater than \tilde{F}_{str} , and that the greater density of the particle surprisingly shifts the rise of \tilde{F}_{str} towards higher δ/a . Studying spheroids and spheres with protruding crowns revealed that the contribution of the particle shape to the viscous contributions to the ARF, namely, \tilde{F}_{vsc} and \tilde{F}_{str} , is generally insignificant. This happens in part due to \tilde{F}_{vsc} and \tilde{F}_{str} being negligible at $\delta/a < 1$, and in part due to the viscous boundary layer extending past the shape features when \tilde{F}_{vsc} and \tilde{F}_{str} become relevant at $\delta/a > 1$. However, for dense particles, extreme asymmetric shape perturbations in the form of sharp crowns can give rise to noticeable viscous contributions to the ARF at $\delta/a \ll 1$.

We also introduce a versatile analytical model that combines the contribution of the microstreaming and viscous scattering to the ARF from the rigid particle model by Doinikov [22] and a scattering contribution due to the particle compressibility from the inviscid model by Yosioka and Kawasima [32]. The hybrid analytical model is in a good agreement with our numerical model that accounts for the particle compressibility and all the viscous effects in the fluid, for all particle materials and sizes considered in the study. The numerical models and the Matlab code for the analytical models used in the study are provided in the Supplemental Material [43].

II. THEORY

The motion of a viscous fluid is governed by the compressible Navier-Stokes equations

$$\rho \left[\frac{\partial \mathbf{v}}{\partial t} + (\mathbf{v} \cdot \nabla) \mathbf{v} \right] = -\nabla p + \eta \nabla^2 \mathbf{v} + \left(\eta_{\text{B}} + \frac{\eta}{3} \right) \nabla (\nabla \cdot \mathbf{v}) \quad (1)$$

and the continuity equation

$$\frac{\partial \rho}{\partial t} = -\nabla \cdot (\rho \mathbf{v}), \quad (2)$$

with the dynamic viscosity η and the bulk viscosity η_{B} . The density ρ is assumed to be a function of pressure p only (barotropic fluid), and \mathbf{v} represents the velocity field. The particle is assumed to be linear elastic solid.

The equations are linearized using the regular perturbation approach [44]. Accordingly, the physical fields are expanded in a series $\square = \square_0 + \square_1 + \square_2 + \dots$, where \square represents the field, while the subscript denotes the respective order. The amplitude of the first-order velocity \mathbf{v}_1 is assumed to be small with respect to the speed of sound c_f (small Mach number assumption).

The theory could be extended to cover thermal effects, by adding temperature as an unknown variable, and the equation of energy conservation to the set of governing equations, as done in Refs. [35,45]. The particle would then need to be modeled as a thermoelastic solid.

A. First-order (acoustic) problem

For a fluid quiescent at the zeroth order ($\mathbf{v}_0 = \mathbf{0}$), the substitution of the first-order perturbed fields into the governing equations yields the following set of first-order equations:

$$\rho_0 \frac{\partial \mathbf{v}_1}{\partial t} = -\nabla p_1 + \eta \nabla^2 \mathbf{v}_1 + \left(\eta_{\text{B}} + \frac{\eta}{3} \right) \nabla (\nabla \cdot \mathbf{v}_1), \quad (3)$$

$$\frac{\partial \rho_1}{\partial t} = -\rho_0 \nabla \cdot \mathbf{v}_1, \quad (4)$$

with the equilibrium density ρ_0 . The equation of state,

$$\rho_1 = \frac{1}{c_f^2} p_1, \quad (5)$$

is connecting the first-order density with the first-order pressure. The first-order fields are assumed to have a harmonic time dependency with the factor of $e^{i\omega t}$, where $\omega = 2\pi f$ is the angular frequency and i the imaginary unit.

The acoustic fields, comprising velocity \mathbf{v}_1 and pressure p_1 , are assumed to be the sums of the corresponding background fields (bg) and scattered fields (sc), namely, $\square_1 = \square_1^{\text{bg}} + \square_1^{\text{sc}}$. We assume a one-dimensional plane standing wave along the z direction of the cylindrical coordinate system (r, θ, z) , defined through the background velocity field

$$\mathbf{v}_1^{\text{bg}} = \text{Re} \left[\frac{\varphi_a}{2} i k (e^{ikz} - e^{-ikz}) e^{i\omega t} \right] \mathbf{e}_z, \quad (6)$$

with the corresponding velocity potential amplitude

$$\varphi_a = -\frac{p_a}{i\omega\rho_0 + \left(\eta_{\text{B}} + \frac{4}{3}\eta \right) k^2}, \quad (7)$$

with the pressure amplitude p_a , and the wave number

$$k = \frac{\omega}{c_f} - \alpha i, \quad (8)$$

with the attenuation coefficient for viscous fluids [46]

$$\alpha = \frac{\omega^2 \eta}{2c_f^3 \rho_0} \left(\frac{\eta_{\text{B}}}{\eta} + \frac{4}{3} \right). \quad (9)$$

At the fluid-solid interfaces, the continuity of velocity and stress are imposed. The first-order fields are assumed to converge to the background fields far from the particles, in an unbounded fluid.

B. Second-order (streaming) problem

Applying the perturbation theory up to second order to the governing equations and taking the time average over an

oscillation period T , defined as $\langle \square \rangle = \frac{1}{T} \int_T \square dt$, leads to the equations of acoustic streaming [47]:

$$\nabla \langle p_2 \rangle - \eta \nabla^2 \langle \mathbf{v}_2 \rangle = -\rho_0 \nabla \cdot \langle \mathbf{v}_1 \mathbf{v}_1 \rangle, \quad (10)$$

$$\nabla \cdot \langle \mathbf{v}_2 \rangle = 0. \quad (11)$$

Whenever two vectors are side by side, as $\langle \mathbf{v}_1 \mathbf{v}_1 \rangle$ are in Eq. (10), the tensor product is implied. In Eqs. (10) and (11), we consider the streaming field to be incompressible, in line with related studies [48].

At the second order, the no-slip boundary condition is imposed on the Lagrangian velocity of the fluid at the fluid-solid interface; the Lagrangian velocity is defined as the summation of the Eulerian streaming velocity $\langle \mathbf{v}_2 \rangle$ and the Stokes drift [49,50]

$$\mathbf{v}_{\text{SD}} = \left\langle \left(\int \mathbf{v}_1 dt \cdot \nabla \right) \mathbf{v}_1 \right\rangle, \quad (12)$$

leading to the boundary condition

$$\langle \mathbf{v}_2 \rangle = -\mathbf{v}_{\text{SD}} \quad \text{at the interface.} \quad (13)$$

The environmental streaming due to the attenuation of the background field in the absence of the particle is assumed negligible for the standing wave [22,39] and was neglected also in the present study. Accordingly, the no-slip condition is applied to the fluid at the outer boundary.

The above derivation is meaningful only as long as the perturbation theory is valid and as long as the streaming remains laminar.

Experimentally, the standing wave is usually established inside a microfluidic device, where the geometry-dependent [25,51,52] Rayleigh streaming [17,53] appears due to the presence of walls. We do not consider this type of streaming here, as it could be computed without the presence of the particles and then used to predict the cumulative force on an individual particle (e.g., [13,54]).

C. Acoustic radiation force

The time-averaged ARF on a particle is defined as the mapping of a stress tensor $\boldsymbol{\sigma}$ onto the outward pointing surface normal $\mathbf{n}(t)$, integrated over surface $S(t)$ of a particle undergoing oscillations, namely,

$$\mathbf{F}_{\text{rad}} = \left\langle \int_{S(t)} \boldsymbol{\sigma} \cdot \mathbf{n}(t) dS \right\rangle. \quad (14)$$

It has been proven (see [45] for the range of validity) that the second-order expression for the ARF can also be written as [22,45]

$$\mathbf{F}_{\text{rad}} = \int_{S_0} [(\boldsymbol{\sigma}_2) - \rho_0 \langle \mathbf{v}_1 \mathbf{v}_1 \rangle] \cdot \mathbf{n}_0 dS, \quad (15)$$

where the difference between the time-averaged second-order incompressible stress tensor

$$\langle \boldsymbol{\sigma}_2 \rangle = -\langle p_2 \rangle \mathbf{I} + \eta (\nabla \langle \mathbf{v}_2 \rangle + (\nabla \langle \mathbf{v}_2 \rangle)^T) \quad (16)$$

and the Reynolds stress $\rho_0 \langle \mathbf{v}_1 \mathbf{v}_1 \rangle$ is mapped onto the normal \mathbf{n}_0 pointing out of the arbitrary static surface S_0 enclosing the particle, and integrated over S_0 . The microstreaming is,

together with other viscous effects at the second order, contained in the stress tensor $\langle \boldsymbol{\sigma}_2 \rangle$, while the first-order viscous scattering effects also contribute to \mathbf{v}_1 .

Some studies [42,45] neglect the viscosity at the second order, but account for the viscous scattering effects. This results in a simplified expression for $\langle p_2 \rangle$ from Eq. (16), namely,

$$\langle p_2 \rangle^{\text{noStr}} = \frac{1}{2\rho_0 c_f^2} \langle p_1^2 \rangle - \frac{1}{2} \rho_0 \langle \mathbf{v}_1 \cdot \mathbf{v}_1 \rangle, \quad (17)$$

and in the simplified expression for the ARF,

$$\mathbf{F}_{\text{rad}}^{\text{noStr}} = \int_{S_0} \left[\left(\frac{1}{2\rho_0 c_f^2} \langle p_1^2 \rangle - \frac{1}{2} \rho_0 \langle \mathbf{v}_1 \cdot \mathbf{v}_1 \rangle \right) \mathbf{I} - \rho_0 \langle \mathbf{v}_1 \mathbf{v}_1 \rangle \right] \cdot \mathbf{n}_0 dS. \quad (18)$$

Neglecting viscosity already at the first order leads to the inviscid first-order fields in Eq. (18) that are obtained by neglecting the viscosity ($\eta = \eta_B = 0$) in Eq. (3). If in addition, the particle is assumed to be spherical and small compared to the acoustic wavelength of a standing wave along the z direction, Eq. (18) reduces to the well-known expression derived by Yosioka and Kawasima [32] and Gor'kov [33], namely,

$$\mathbf{F}_{\text{yos}} = F_{\text{yos}} \mathbf{e}_z = 3V \Phi k E_{\text{ac}} \sin(2kz) \mathbf{e}_z, \quad (19)$$

with the particle volume $V = 4\pi a^3/3$, the acoustic contrast factor Φ that represents the density and compressibility contrast between the fluid and the particle (reference values are given in Table I), the ideal wave number $k = \omega/c_f$, and the acoustic energy density $E_{\text{ac}} = p_a^2/(4\rho_0 c_f^2)$. For the purpose of normalization, we also define

$$F_{\text{yos}}^{\text{max}} = 3V \Phi k E_{\text{ac}}, \quad (20)$$

which corresponds to the amplitude of F_{yos} , evaluated in the middle between the pressure node and antinode of a standing wave, namely, at $z = \lambda/8$, with the acoustic wavelength $\lambda = c_f/f$.

III. NUMERICAL MODEL

The numerical model that solves the axisymmetric first- and second-order problems is based on Ref. [39]. The model is implemented in COMSOL Multiphysics v. 5.6 [58] and is available with all the supporting functions in the Supplemental Material [43]. The first-order equations (3)–(5) are defined through the adiabatic form of the Thermoviscous Acoustics (ta) physics interface from the Acoustics Module. The Solid Mechanics (solid) interface is used to model the linear elastic solid spherical particles and is connected to the Thermoviscous Acoustics (ta) interface via the Thermoviscous Acoustic-Solid Interaction interface. The background acoustic field from Eq. (6) is imposed directly in the Thermoviscous Acoustics (ta) interface. The perfectly matched layer (PML) is assigned to the outermost subdomain of the fluid domain (green region in Fig. 1). The multiphysics first-order problem is solved in the frequency domain, using the Frequency Domain study.

The second-order streaming equations (10) and (11) are solved via a modified Creeping Flow (spf) interface of the CFD Module. This physics interface is assigned to the fluid domain, excluding the region of the PML (green region in

TABLE I. The material parameters for water (H₂O) [45], polystyrene (PS) [55], red blood cell (RBC) [56,57], glass [55], titanium (Ti) [55], copper (Cu) [55], and gold (Au) [55]. The acoustic contrast factor Φ for a single particle in water is computed using Eq. (30c) of Ref. [16] and is positive for all materials in the current study.

	H ₂ O	Unit		PS	RBC	Glass	Ti	Cu	Au	Unit
ρ_0	996.6	kg m ⁻³	ρ_p	1050	1100	2240	4480	8930	19 700	kg m ⁻³
c_f	1502	m s ⁻¹	c_p	2400	1658	5100	6100	5010	3240	m s ⁻¹
η	0.854	mPa s	c_s	1150	30.2	2800	3100	2270	1280	m s ⁻¹
η_B	2.4	mPa s	Φ	0.17	0.12	0.54	0.68	0.75	0.79	—

Fig. 1). The spatial variation of the Reynolds stress, i.e., the right-hand side of Eq. (10), is added as a Volume Force to the Creeping Flow (spf) interface and contributes over the whole fluid domain. At the fluid-particle interface, we apply the negative Stokes drift from Eq. (12) through a Wall boundary condition, enforcing the no-slip boundary condition, while accounting for the movement of the interface at the first order. To constrain the formulated streaming problem, we set the second-order pressure field to a constant value at an arbitrary point in the fluid domain, using the Pressure Point Constraint. Our formulation implies that the streaming fields are already steady, and accordingly, we solve the streaming problem with the Stationary study. The latter takes into account the solutions of the first-order Frequency Domain study, to determine the Stokes drift and the Reynolds stress that are used in the streaming problem.

In order to analyze the influence of the fluid viscosity on the scattering at the particle, we also use an inviscid first-

order numerical model. The inviscid model is built in the same way as the first-order part of the viscous model, with the only difference being that the Thermoviscous Acoustics (ta) interface is replaced by the Pressure Acoustics (acpr) interface, and the fluid-solid coupling is implemented via the Acoustic-Solid Interaction interface. The Pressure Acoustics interface solves only the inviscid first-order problem that is derived from Eqs. (3)–(5), by setting $\eta = \eta_B = 0$ in Eq. (3).

The forces computed with the numerical models are summarized in Fig. 1(b) and are defined as follows: “ ARF_{str} ” is the total ARF including the microstreaming and is computed using Eq. (15) in the viscous model, specifically $ARF_{str} = \mathbf{F}_{rad} \cdot \mathbf{e}_z$; “ ARF_{noStr} ” is the ARF that accounts for the viscous scattering effects (i.e., viscosity at the first order), but neglects the microstreaming, and is computed using Eq. (18) in the viscous model, namely, $ARF_{noStr} = \mathbf{F}_{rad}^{noStr} \cdot \mathbf{e}_z$; “ ARF_{inv} ” is the ARF for an inviscid fluid, also computed using Eq. (18), but in the inviscid model. The surface integral in Eq. (15) is

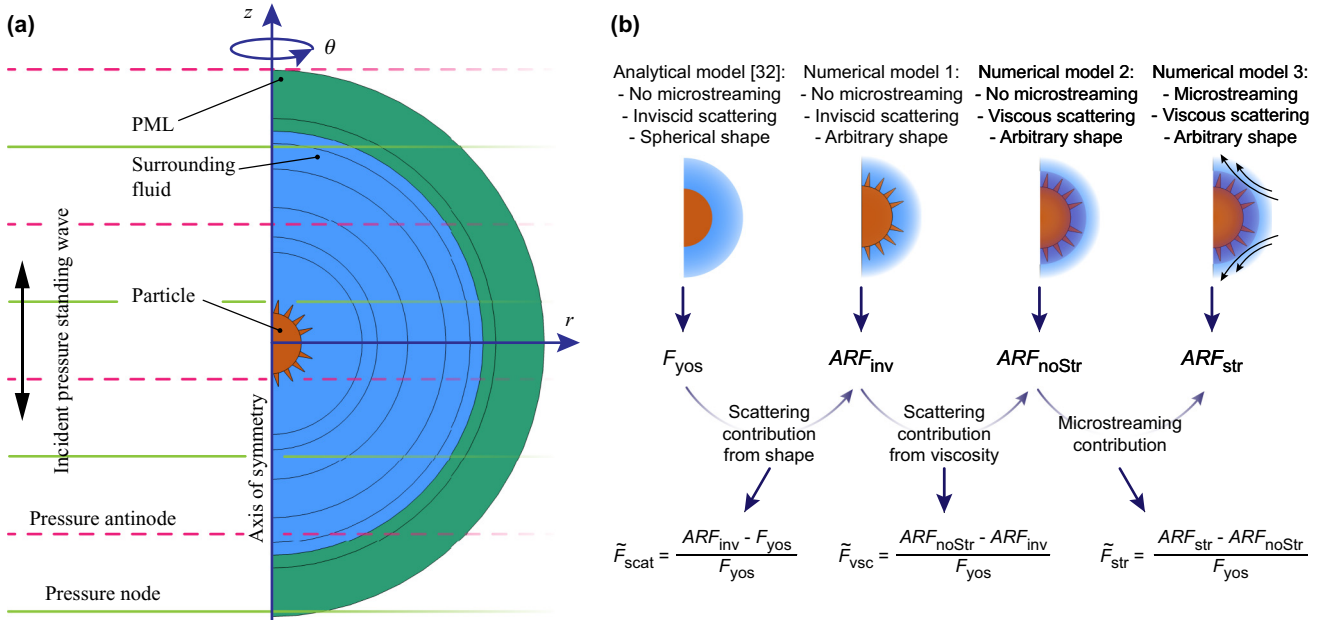


FIG. 1. (a) The geometry of the axisymmetric numerical model of a spherical particle with protruding crowns. The model is parametrized in the cylindrical coordinate system (r, θ, z) , with the z axis parallel to the direction of the pressure gradient of the one-dimensional incident standing wave. A perfectly matched layer (PML) surrounds the fluid domain. (b) The gradual relaxation in the modeling assumptions from the analytical model for the ARF on a sphere in an inviscid fluid by Yosioka and Kawasima [32], through numerical models that add the arbitrary axisymmetric shape deviations (ARF_{inv}) and the viscous scattering (ARF_{noStr}), to the fully viscous numerical model that accounts for the microstreaming (ARF_{str}). This incremental increase in the model complexity allows us to define normalized contributions of the individual effect to the fully viscous (total) ARF, namely, the inviscid scattering contribution due to shape \tilde{F}_{scat} , the viscous scattering contribution \tilde{F}_{vsc} , and the microstreaming contribution \tilde{F}_{str} .

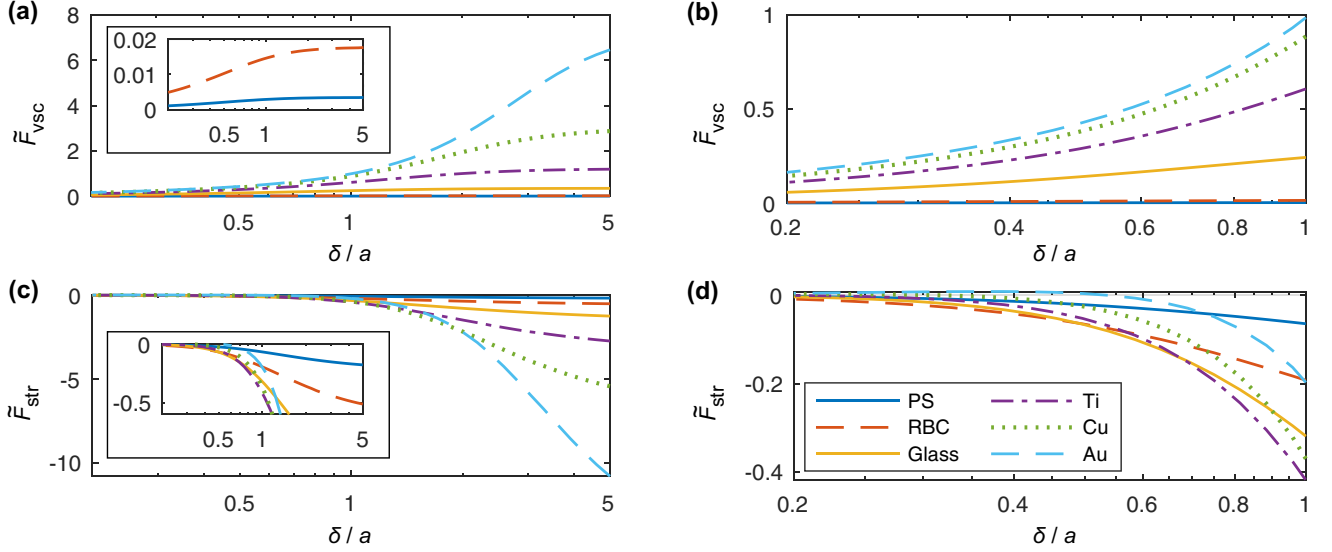


FIG. 2. Influence of the material of a spherical particle on the ARF with respect to the particle radius a . [(a), (b)] The viscous scattering contribution to the ARF (\tilde{F}_{vsc}) and [(c), (d)] the microstreaming contribution to the ARF (\tilde{F}_{str}). The particle is in water, positioned in the middle between the pressure node and antinode of a standing wave with a frequency of 500 kHz, yielding $\delta = 0.74 \mu\text{m}$. The particle materials include polystyrene (PS), red blood cell (RBC), glass, titanium (Ti), copper (Cu), and gold (Au), in order of increasing density. The insets in (a) and (c) feature a reduced range on the vertical axis, to highlight the magnitude of viscous contributions for PS and RBC.

for ARF_{str} evaluated at an arbitrary surface surrounding the particle. However, for evaluating ARF_{noStr} through Eq. (18), the integration surface needs to be at a sufficient distance from the particle surface — at least $\sim 5\delta$ [42,59] — since Eq. (18) assumes an irrotational first-order velocity field, which holds true only outside the viscous boundary layer around the particle.

IV. RESULTS

To study the influence of the particle material and shape on the ARF and microstreaming, we decompose the total ARF from the viscous numerical model that accounts for the microstreaming into several parts:

$$ARF_{\text{str}}\mathbf{e}_z = [(\tilde{F}_{\text{str}} + \tilde{F}_{\text{vsc}} + \tilde{F}_{\text{scat}})F_{\text{yos}}^{\text{max}} + F_{\text{yos}}]\mathbf{e}_z, \quad (21)$$

with the microstreaming contribution \tilde{F}_{str} to the total ARF on a particle defined as

$$\tilde{F}_{\text{str}} = \frac{ARF_{\text{str}} - ARF_{\text{noStr}}}{F_{\text{yos}}^{\text{max}}}, \quad (22)$$

the viscous scattering contribution \tilde{F}_{vsc} , arising due to the first-order viscous effects, as

$$\tilde{F}_{\text{vsc}} = \frac{ARF_{\text{noStr}} - ARF_{\text{inv}}}{F_{\text{yos}}^{\text{max}}}, \quad (23)$$

and the last contribution, \tilde{F}_{scat} , comes from the influence of the particle shape on the inviscid scattering and is evaluated as

$$\tilde{F}_{\text{scat}} = \frac{ARF_{\text{inv}} - F_{\text{yos}}}{F_{\text{yos}}^{\text{max}}}. \quad (24)$$

For all the results, the fluid surrounding the particle is water with material properties given in Table I. The standing wave is defined through the frequency $f = 500 \text{ kHz}$ and the pressure

amplitude $p_a = 500 \text{ kPa}$, and the particle is always positioned in the middle between the pressure node and antinode, except in Sec. IV C, where the dependency of the ARF on the particle position in a standing wave is discussed. For the given frequency, $\delta = 0.74 \mu\text{m}$ in water. The particle materials are, in the order of increasing density, polystyrene (PS), red blood cell (RBC), glass, titanium (Ti), copper (Cu), and gold (Au), with properties given in Table I.

A. Influence of the particle material

The analysis of the ARF on a spherical particle of different materials in Fig. 2 reveals that the viscous contributions to the ARF, namely, \tilde{F}_{vsc} and \tilde{F}_{str} , become significant with respect to the inviscid force (F_{yos}) once the particle radius is comparable to or smaller than the viscous boundary layer thickness ($a \lesssim \delta$). For the smallest particle, at $a = \delta/5$, the microstreaming contribution \tilde{F}_{str} in Fig. 2(c) is more significant than the viscous scattering contribution \tilde{F}_{vsc} in Fig. 2(a), for all analyzed materials. However, at the particle size of $a \approx 2\delta$, the viscous scattering contribution \tilde{F}_{vsc} is dominant for most particle materials [Figs. 2(b) and 2(d)].

The particle materials that we consider all have a positive acoustic contrast factor Φ (Table I), which in combination with the inviscid ARF from Eq. (19) yields the pressure node to be the equilibrium position of the particles. However, the microstreaming contribution to the ARF, which is negative relative to the inviscid ARF [Figs. 2(c) and 2(d)], can cause an inversion of the sign of the ARF with the increase in δ/a , as demonstrated in Fig. 3 for gold, copper, and titanium. This phenomenon was investigated before [22,39,60], and results in the shift of the equilibrium position of a particle from a pressure node to a pressure antinode.

From Figs. 2(a) and 2(c) it follows that the denser the particle, the larger the relative contribution of both viscous effects

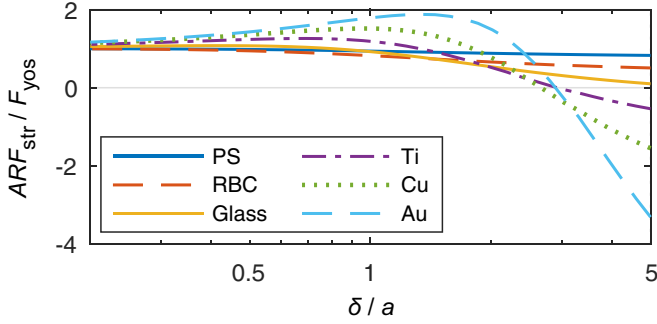


FIG. 3. The ARF from our numerical model that includes the viscous scattering and the microstreaming (ARF_{str}) normalized by the inviscid ARF [32] with respect to the particle radius a . The particle is in water, positioned in the middle between the pressure node and antinode of a standing wave with a frequency of 500 kHz, yielding $\delta = 0.74 \mu\text{m}$. The particle materials include polystyrene (PS), red blood cell (RBC), glass, titanium (Ti), copper (Cu), and gold (Au), in order of increasing density.

at $a \ll \delta$. In the intermediate particle size range [$5\delta \geq a \geq \delta$ in Figs. 2(b) and 2(d)] the viscous scattering contribution \tilde{F}_{vsc} keeps increasing with the particle density; but the increase in the particle density surprisingly shifts the rise of the microstreaming contribution \tilde{F}_{str} towards higher δ/a . We further explore the shift in the rise of \tilde{F}_{str} in Fig. 4(a), which shows the maximal instantaneous first-order velocity magnitude near the particle with respect to the decreasing particle size. The instantaneous first-order velocity is the first-order velocity field that is in phase with the background acoustic pressure field. The whole range of the investigated materials exhibits a local minimum of the maximal instantaneous first-order velocity magnitude, denoted with the vertical lines in Fig. 4(a). Investigating the spatial location of the maximal instantaneous first-order velocity magnitude, such as in Figs. 5(a)–5(c) for a copper particle, reveals that there are two local maxima, one near the equator ($z \approx 0$) that decreases in magnitude as δ/a increases, and the second near the poles ($z = \pm a$) that increases in magnitude as δ/a increases. The characteristic particle size at which the magnitudes of the instantaneous first-order velocity at the equator and the poles cross over corresponds to the local minimum of the maximal instantaneous first-order velocity magnitude in Fig. 4(a) and decreases with the increase in the particle density. This feature of the first-order velocity field could explain the rise of \tilde{F}_{str} in Fig. 2(d) that is analogously shifted to a smaller particle size as the density of the particle is increased.

The particle size yielding a maximal streaming velocity for each of the materials in Fig. 4(b) decreases with the increase in the particle density. The corresponding Eulerian streaming patterns for a copper particle, shown in Figs. 5(d)–5(f), reveal that the streaming pattern also undergoes a transition, as the narrow vortices near the particle at $\delta/a < 1$ [Fig. 5(d)] gradually expand and in the end dominate the microstreaming pattern at $\delta/a > 1$ [Fig. 5(f)]. This transition in the streaming pattern is summarized through the streaming velocity profiles for different materials in Figs. 5(g)–5(i), which additionally reveal that as the decrease in the particle size leads to an increase in the magnitude of the radial component of the streaming velocity near the particle, it also leads to a more

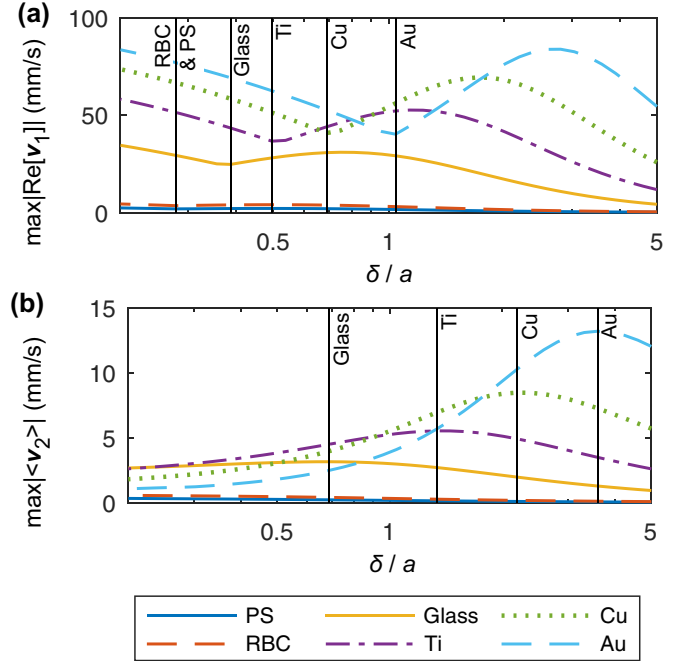


FIG. 4. Influence of the size and material of a spherical particle on the instantaneous first-order velocity and microstreaming with respect to the particle radius a . (a) The maximal magnitude of the instantaneous first-order velocity in the fluid and (b) the maximal magnitude of the acoustic streaming velocity in the fluid with respect to the particle radius a . The particle is in water, positioned in the middle between the pressure node and antinode of a standing wave with an amplitude of 500 kPa and a frequency of 500 kHz, yielding $\delta = 0.74 \mu\text{m}$. The particle materials include polystyrene (PS), red blood cell (RBC), glass, titanium (Ti), copper (Cu), and gold (Au), in order of increasing density. The vertical lines in (a) mark the point of transition in the location of the maximum instantaneous first-order velocity, while in (b) they mark the point of maximum streaming velocity (maxima for RBC and PS are outside the investigated size range).

significant decay of the streaming velocity with the distance away from the particle surface.

When comparing the streaming patterns around a copper [Figs. 5(d) and 5(f)] and a polystyrene [Figs. 6(c) and 6(d)] particle, we see that the inner vortex near the particle surface is at $\delta/a = 0.2$ broader for polystyrene, as indicated with the velocity profile in Fig. 5(g). The outer streaming pattern is less defined for polystyrene. At $\delta/a = 5$, the streaming patterns around the polystyrene and the copper particle look very similar; however, the streaming velocity is more than two orders of magnitude lower for polystyrene. The same trend is visible in the comparison of instantaneous first-order velocity [Figs. 5(a) and 5(c) and Figs. 6(a) and 6(b)].

The comparison of the first- and second-order velocities in Fig. 4 indicates that the validity of the applied perturbation approach could be compromised, in particular for small and dense particles, since the maximal second-order streaming velocity is rising relative to the maximal first-order velocity as the particle gets smaller and denser. This could mean that some combinations of material and geometry no longer satisfy the underlying assumption of the perturbation approach, namely, that second-order quantities are an order

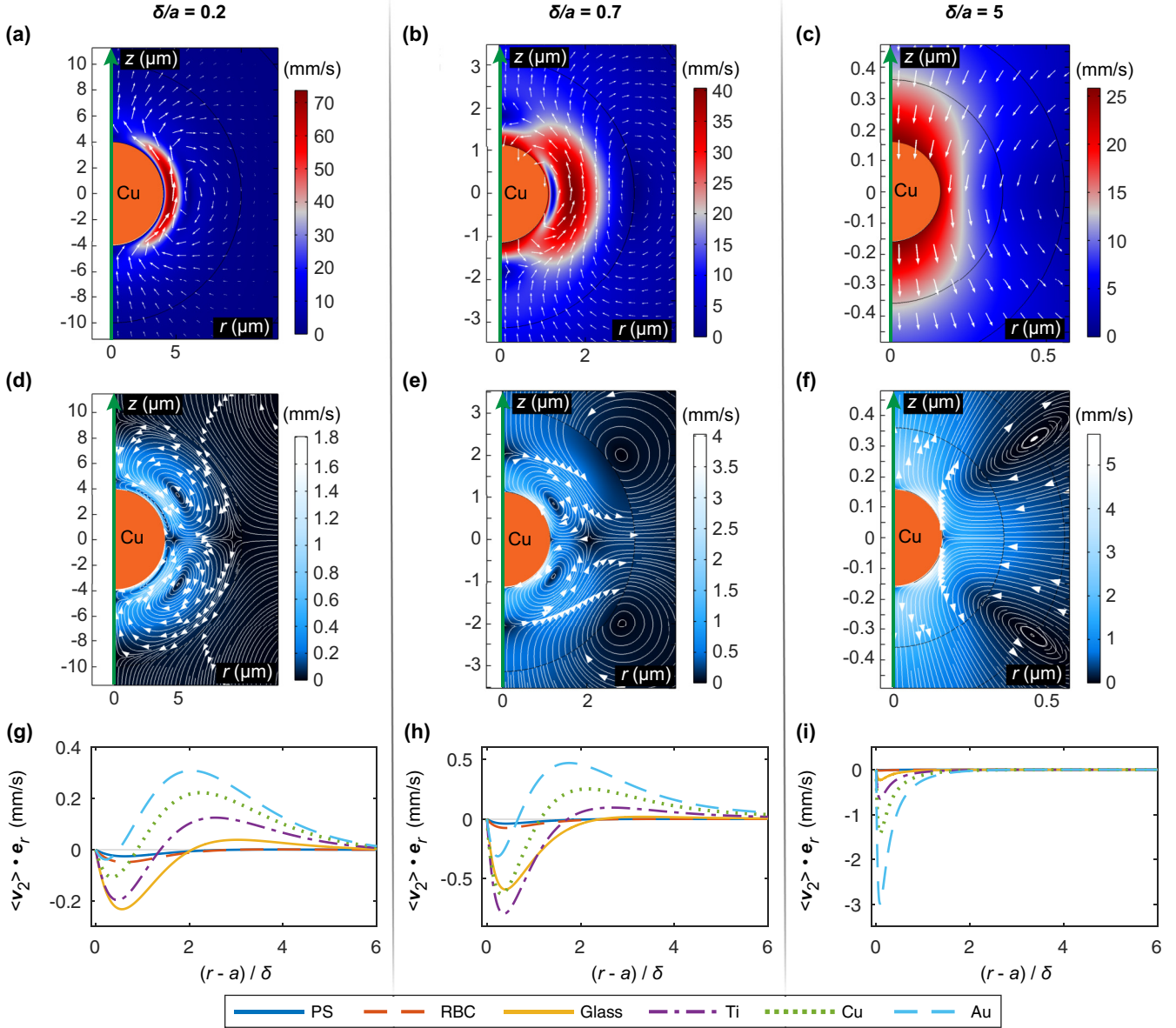


FIG. 5. Influence of the size and material of a spherical particle on the instantaneous first-order velocity and microstreaming. [(a)–(c)] The instantaneous first-order velocity field around a copper particle and [(d)–(f)] the corresponding Eulerian streaming patterns. [(g)–(i)] The profiles of the r component of the streaming velocity plotted along the r axis, at $z = 0$, and starting at the particle surface ($r = a$). The particle is in all cases in water, positioned in the middle between the pressure node and antinode of a standing wave with an amplitude of 500 kPa and a frequency of 500 kHz, yielding $\delta = 0.74 \mu\text{m}$. The particle materials include polystyrene (PS), red blood cell (RBC), glass, titanium (Ti), copper (Cu), and gold (Au), in order of increasing density. The arrows in (a)–(c) are scaled logarithmically with the magnitude of the instantaneous first-order velocity, while they are normalized in (d)–(f). [(a), (d), (g)] $\delta/a = 0.2$; [(b), (e), (h)] $\delta/a = 0.7$; [(c), (f), (i)] $\delta/a = 5$.

of magnitude smaller than their first-order counterparts. The streaming velocity field could therefore be influencing the acoustic velocity field. Such breakage of the perturbation theory was observed, for example, in the vicinity of acoustically excited sharp edges, where the streaming velocity reaches high magnitudes [61]. However, further investigation of validity of the perturbation approach is beyond the scope of the current paper.

For a sphere, ARF_{noStr} — the ARF from the viscous numerical model that accounts for the viscous scattering effects, but neglects the microstreaming — should match the force F_{sett} from the first-order viscous model by Settnes and Bruus [42]

that neglects the microstreaming. We compare these forces in Fig. 7(a) and see that the agreement is relatively good, unless the density is too large, as is the case for copper and gold. The difference could originate from simplifications made by Settnes and Bruus [42], for example, limiting the particle deformation to the monopole and the dipole modes, whereas our model considers all the modes. To further validate our results, we analyzed the dependence of ARF_{noStr} on the distance between the particle and the integration surface, which is in our simulations $> 10\delta$; the results (Appendix A) confirm that the distance of $\gtrsim 5\delta$ is sufficient to avoid errors due to the rotational first-order velocity field.

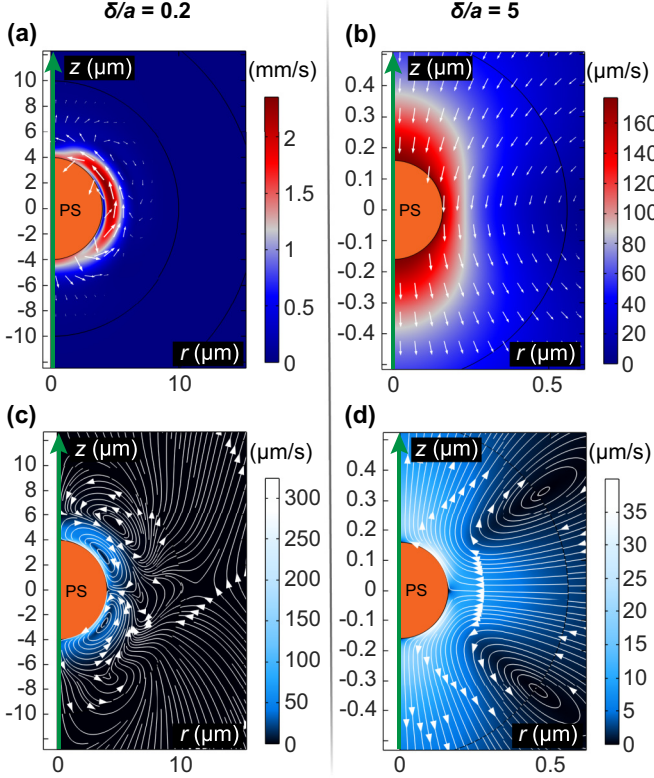


FIG. 6. [(a), (b)] The instantaneous first-order velocity field around a polystyrene particle and [(c), (d)] the corresponding Eulerian streaming patterns. The particle is in all cases in water, positioned in the middle between the pressure node and antinode of a standing wave with an amplitude of 500 kPa and a frequency of 500 kHz, yielding $\delta = 0.74 \mu\text{m}$. The arrows in (a) and (b) are scaled logarithmically with the magnitude of the instantaneous first-order velocity, while they are normalized in (c) and (d). [(a), (c)] $\delta/a = 0.2$; [(b), (d)] $\delta/a = 5$.

The ARF from the viscous numerical model accounting for the microstreaming, namely, ARF_{str} , is in Fig. 7 compared to the force F_{doi} from the model by Doinikov [22] that accounts for the microstreaming, but assumes the particle to be incompressible (F_{doi} is given in Appendix B). Figure 7(b) shows that for dense materials, F_{doi} agrees with our ARF_{str} . However, the less dense materials — polystyrene and red blood cell — for which the compressibility contrast to the surrounding fluid is significantly affecting the ARF, cannot be correctly modeled with the analytical model [22], which is attributed to the inherent assumption of particle incompressibility.

Since the model by Doinikov [22] is the simplest analytical ARF model accounting for the microstreaming around a spherical particle in the Rayleigh limit ($ka \ll 1$), we use it as a basis and try to account for the compressibility of the particle by adding the compressibility contribution from the inviscid model by Yosioka and Kawasima [32], namely,

$$F_{\text{hyb}} = F_{\text{doi}} - V \left[\frac{\rho_0 c_f^2}{\rho_p (c_p^2 - \frac{4}{3} c_s^2)} \right] k E_{\text{ac}} \sin(2kz). \quad (25)$$

The hybrid force F_{hyb} is analyzed in Fig. 7(c), and it indicates that the added compressibility contribution did not affect the

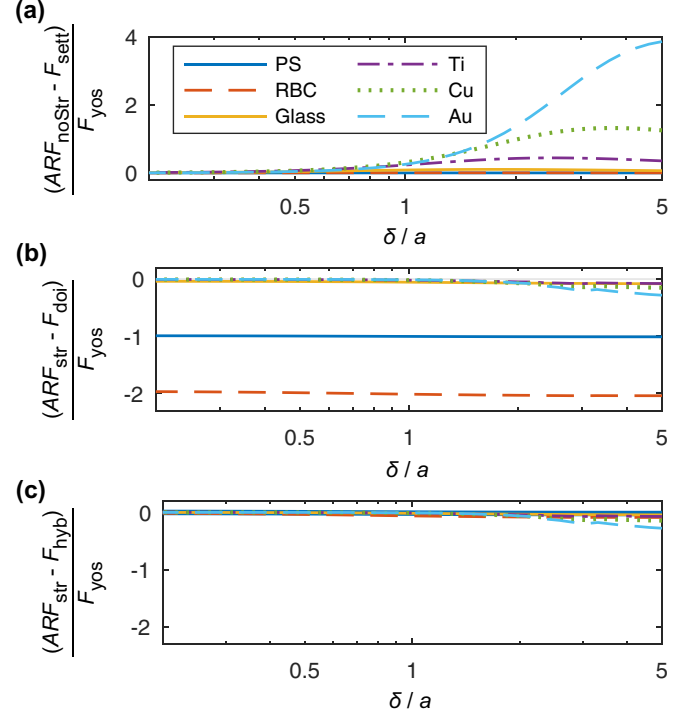


FIG. 7. Comparison between analytical ARF models and the numerically obtained ARF with respect to the particle radius a . (a) The comparison of ARF_{noStr} with the analytical model by Settles and Bruus [42] that accounts for the viscous scattering effects, but neglects the microstreaming (F_{sett}). (b) The comparison of ARF_{str} with the analytical model by Doinikov [22] that accounts for the microstreaming, but assumes a rigid particle (F_{doi}). (c) The comparison between ARF_{str} , and the modified expression for the ARF (F_{hyb}) from Eq. (25). The differences in forces are normalized by the inviscid model (F_{yos}) by Yosioka and Kawasima [32]. The particle is in water, positioned in the middle between the pressure node and antinode of a standing wave with an amplitude of 500 kPa and a frequency of 500 kHz, yielding $\delta = 0.74 \mu\text{m}$. The particle materials include polystyrene (PS), red blood cell (RBC), glass, titanium (Ti), copper (Cu), and gold (Au), in order of increasing density.

dense materials, but it did close the gap between the model by Doinikov [22] and the numerically obtained ARF_{str} for polystyrene and red blood cells.

B. Influence of the particle shape

One of the simplest deviations from the spherical shape is the spheroidal shape, which is also frequently analyzed in the context of the ARF [11,12,62]. Figure 8 shows the influence of the spheroid eccentricity $|\epsilon| = \sqrt{1 - c^2}$, with aspect ratio c between the two semiaxes, on the scattering, viscous scattering, and microstreaming contributions to the ARF, \tilde{F}_{scat} , \tilde{F}_{vsc} , and \tilde{F}_{str} , respectively. The relative scattering contribution due to shape deviation \tilde{F}_{scat} is independent of the δ/a [Figs. 8(a)–8(c)]. The viscous scattering and microstreaming contributions, on the other hand, increase with δ/a , as is already evident from Fig. 2. However, as δ/a increases, \tilde{F}_{vsc} and \tilde{F}_{str} become independent of the spheroid eccentricity [Figs. 8(f) and 8(i)].

The streaming patterns around the prolate and oblate spheroids with eccentricity of $|\epsilon| = 0.95$ in Figs. 9(a) and

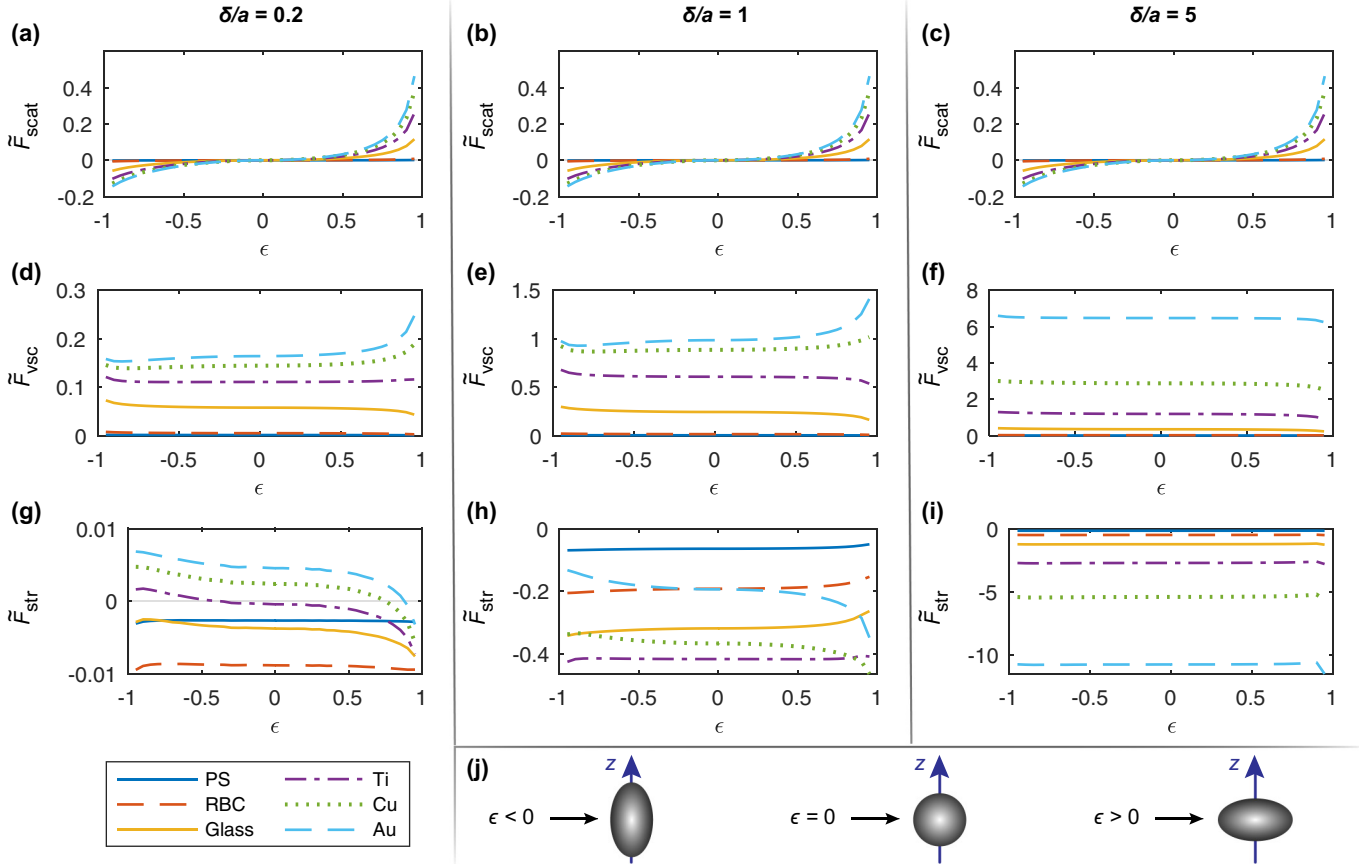


FIG. 8. Influence of a spheroidal particle shape on the ARF and microstreaming with respect to the effective particle radius a . [(a)–(c)] The inviscid scattering contribution to the ARF due to the particle shape ($\tilde{F}_{\text{scat}}^{\text{invisc}}$), [(d)–(f)] the viscous scattering contribution to the ARF ($\tilde{F}_{\text{scat}}^{\text{visc}}$), and [(g)–(i)] the microstreaming contribution to the ARF (\tilde{F}_{str}). The particle is in water, positioned in the middle between the pressure node and antinode of a standing wave with a frequency of 500 kHz, yielding $\delta = 0.74 \mu\text{m}$. The particle materials include polystyrene (PS), red blood cell (RBC), glass, titanium (Ti), copper (Cu), and gold (Au), in order of increasing density. The shape of the spheroid is defined via its eccentricity $|\epsilon| = \sqrt{1 - c^2}$ with aspect ratio c between the two semiaxes aligned with the r and z axes, and ranges from $|\epsilon| = 0$ (sphere) to $|\epsilon| = 0.95$. The volume of the spheroid is constrained to $V = 4\pi a^3/3$. (j) Depending on the sign of ϵ , the spheroid is prolate ($\epsilon < 0$) or oblate ($\epsilon > 0$), while $\epsilon = 0$ corresponds to a sphere with a radius of a .

9(c) show the large influence of the shape, at $\delta/a = 5$, with the prolate spheroid in Fig. 9(c) yielding an additional pair of vortices, compared to the oblate spheroid in Fig. 9(a). The magnitude is also significantly greater for the oblate spheroid [Fig. 9(a)]. However, for a small particle at $\delta/a = 5$ in Figs. 9(b) and 9(d), the streaming patterns for the prolate and oblate spheroid closely resemble each other in shape and magnitude. The patterns also resemble those around a sphere ($|\epsilon| = 0$), in Fig. 5(f), but the magnitude is slightly amplified with the increased eccentricity, no matter the orientation (oblate/prolate).

A more extreme example of shape deviation from the sphere is a sphere with multiple crowns protruding the surface [Fig. 1, Figs. 10(h) and 10(i)]. The sharp edges that form the crowns are known to produce a strong streaming field [61,63–66] or even attract and repel the nearby particles [67–69]. The sharp edge streaming can be exploited for mixing [70,71], pumping [72,73], and similar shapes are known to facilitate propulsion of microswimmers [74,75]. In Fig. 10 we analyze the individual contributions to the total ARF for the multicrown model (Fig. 1), where four 10° angle crowns are

distributed at 20° intervals starting from $r = 0$ on each hemisphere ($z > 0$ and $z < 0$) — “whole,” or only on the upper hemisphere ($z > 0$) — “half.” The parameter L represents the length of an individual crown from the sphere surface as a fraction of the radius \tilde{a} of the underlying sphere. The total volume of the multicrown particle is constrained to $V = 4\pi a^3/3$, making a an effective radius of the particle. The tip of crowns is rounded with a radius of $\tilde{a}/100$, to avoid singularities.

For a dense copper (Cu) particle, we can see from Fig. 10 that the influence of crowns on all the contributions to the ARF [Figs. 10(a)–10(c)], relative to the results for a sphere (“Sphere”), increases with the increasing length of the crowns (L). The contribution of the shape to the inviscid scattering ($\tilde{F}_{\text{scat}}^{\text{invisc}}$) is constant with respect to δ/a , and is magnitude-wise a dominant contribution at $\delta/a \ll 1$. The viscous scattering contribution $\tilde{F}_{\text{scat}}^{\text{visc}}$ experiences minimal boosting influence of the crowns at $\delta/a < 1$, but is decreased for up to $\approx 40\%$ relative to the sphere, at $\delta/a = 5$ [$L = 2$; “half” in Fig. 10(b)]. Furthermore, comparison of “whole” and “half” results in Figs. 10(a) and 10(b) indicates that both of the scattering contributions are increasing also with the overall amount of

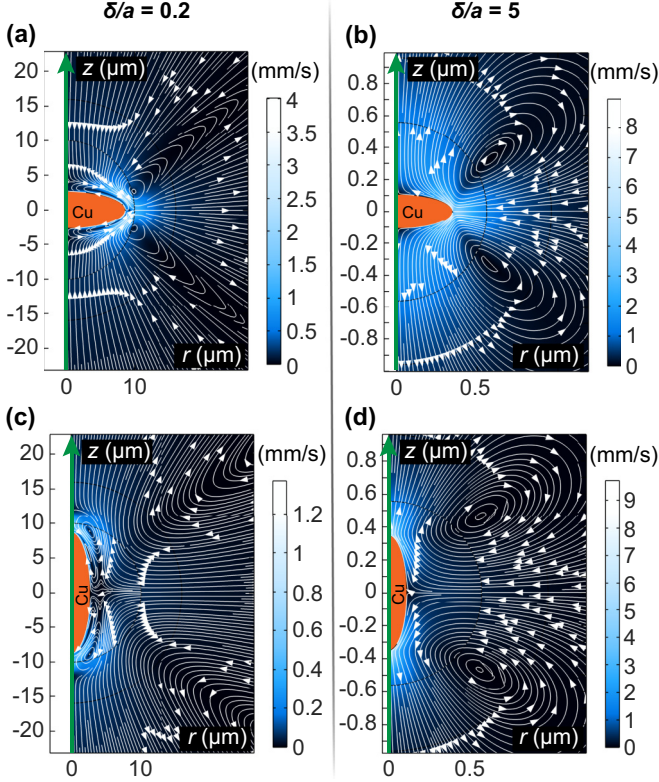


FIG. 9. Influence of the orientation and size of a copper spheroidal particle on the microstreaming. [(a)–(d)] The Eulerian streaming patterns around the copper particle. [(a), (b)] Oblate spheroid with eccentricity $|\epsilon| = 0.95$ and [(c), (d)] prolate spheroid with eccentricity $|\epsilon| = 0.95$. The particle is in all cases in water, positioned in the middle between the pressure node and antinode of a standing wave with an amplitude of 500 kPa and a frequency of 500 kHz, yielding $\delta = 0.74 \mu\text{m}$. The arrows in (a)–(d) are normalized. [(a), (c)] $\delta/a = 0.2$; [(b), (d)] $\delta/a = 5$.

crowns. In contrast, the microstreaming contribution \tilde{F}_{str} increases with the increase in the asymmetry of the crowns [Fig. 10(c)]. At $\delta/a = 5$, the crowns decrease \tilde{F}_{str} for up to $\approx 20\%$ relative to the sphere [$L = 2$; “half” in Fig. 10(c)]. Interestingly, particles with asymmetric placement of crowns (“half”) also influence \tilde{F}_{str} at $\delta/a \ll 1$ [Fig. 10(c)], which probably stems from the regular sharp-edge streaming that propels the particle similarly to how the microswimmers from Kaynak *et al.* [75] are propelled. The streaming pattern at $\delta/a = 0.2$, in Fig. 10(f), indicates that the streaming velocity is indeed the highest at the tip of one of the crowns, and that it follows the well-known pattern of the outflow from the tip with two vortices on each side [63,66]. The crown producing the strongest streaming field is the crown that is most parallel to the r axis. Since the background first-order velocity is aligned with the z axis, this implies that mainly the first-order velocity component that is perpendicular to the crown is responsible for the observed sharp-edge streaming [Fig. 10(d)].

The outer streaming pattern surrounding a multicrown particle at $\delta/a = 0.2$ in Fig. 10(f) generally resembles the pattern around the oblate spheroid in Fig. 9(a), but the crown provides ~ 6 -fold increase in the streaming velocity magnitude

compared to the oblate spheroid, and ~ 13 -fold increase compared to the sphere in Fig. 5(d). At $\delta/a = 5$, the magnitude of the streaming velocity is comparable to the magnitude at $\delta/a = 0.2$, but the pattern becomes more similar to that of the sphere [Fig. 5(f)] and the spheroid [Figs. 9(b) and 9(d)]. Ovchinnikov *et al.* [63] and Zhang *et al.* [61] predicted that the streaming around sharp edges is not affected by the geometry of the sharp edge tip, as long as the geometrical features are smaller than the thickness of the viscous boundary layer. This implies that the geometry of the particle, when the particle and all its geometrical features are small compared to δ , is not significantly affecting the microstreaming pattern in the $\delta/a > 1$ range, as confirmed by comparing the microstreaming patterns for the multicrown model from Fig. 10(g) and the sphere model from Fig. 5(f). However, for $\delta/a \gg 1$, the differences between the sphere and the multicrown model in terms of the streaming pattern and the \tilde{F}_{str} would probably decrease further.

The particles of lower density, such as polystyrene in Fig. 11, experience much lower relative contributions already for a sphere (Fig. 2). We see from Fig. 11 that the addition of crowns affects these contributions in the same manner as it does for the denser copper particle in Fig. 10, but the contributions in the end do not significantly influence the total ARF in the investigated range.

C. Influence of the particle position in the standing wave

The equilibrium position of a particle in a standing wave is ultimately defined by the spatial dependency of the acoustic radiation force. For an inviscid fluid, this dependency follows from Eq. (19) as $\sin(2kz)$, with pressure node at $z = \lambda/4$ and pressure antinodes (velocity nodes) at $z = 0$ and $z = \lambda/2$. While ARF acting on a sphere in a viscous fluid still retains the same spatial dependency [39], the deviations in shape have so-far unknown influence on the spatial dependency of the ARF in a viscous fluid. In Fig. 12 we explore this dependency and show that the addition of an asymmetric multicrown structure (“half” with $L = 1$) to the spherical copper particle shifts the particle’s equilibrium position away from the pressure node. Comparing the behavior at $\delta/a = 0.5$ and $\delta/a = 1$ reveals that the asymmetry influences the equilibrium position more significantly in the intermediate δ/a region, where the geometrical features are not small compared to δ .

The spatial dependency of relative force contributions, analyzed in Fig. 13, indicates the streaming contribution as the only contribution with a spatial dependency deviating from $\sin(2kz)$, and consequently responsible for the shift in the equilibrium position of the asymmetric multicrown particle. The spatial dependency of \tilde{F}_{str} at $\delta/a = 0.5$, showing maximum at the location of the pressure node (velocity antinode), reinforces our theory that the sharp-edge streaming is responsible for the deviation in the ARF at $\delta/a < 1$, since the sharp-edge streaming intensifies as the first-order velocity increases, and in a standing wave, the first-order velocity is maximal at the pressure node.

V. CONCLUSION

We expanded a previously validated numerical model [39] to investigate the influence of the shape and material on the

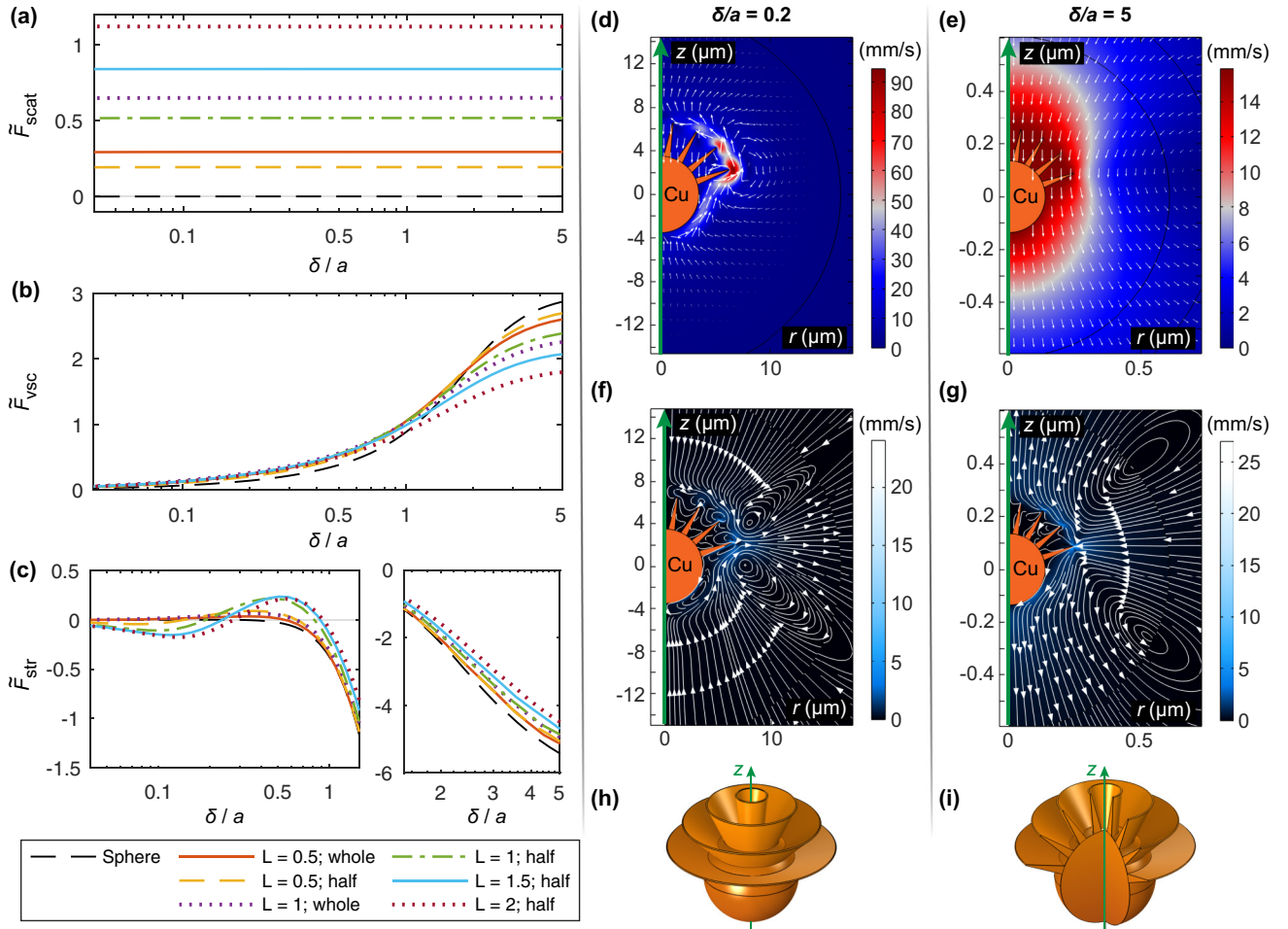


FIG. 10. Influence of a multicrown particle shape on the ARF and microstreaming with respect to the effective particle radius a . (a) The inviscid scattering contribution to the ARF due to the particle shape (\tilde{F}_{scat}), (b) the viscous scattering contribution to the ARF (\tilde{F}_{vsc}), and (c) the microstreaming contribution to the ARF (\tilde{F}_{str}). The copper (Cu) particle is in water, positioned in the middle between the pressure node and antinode of a standing wave with an amplitude of 500 kPa and a frequency of 500 kHz, yielding $\delta = 0.74 \mu\text{m}$. The variations of the multicrown shape include eight crowns placed symmetrically to the $z = 0$ plane on $z > 0$ and $z < 0$ hemispheres, with a 20° step from the $z = 0$ plane (“whole”), as depicted in Fig. 1; only four crowns on the $z > 0$ hemisphere (“half”), as depicted in (d)–(g); crown length L from the sphere surface is varied between $0.5\tilde{a}$, $1\tilde{a}$, $1.5\tilde{a}$, and $2\tilde{a}$, with \tilde{a} defined as the radius of the base sphere on which the crowns are attached. The total volume of the multicrown particle is constrained to $V = 4\pi a^3/3$. The angle of an individual crown is constrained to 10° . [(d), (e)] The instantaneous first-order velocity field around the copper particle and [(f), (g)] the corresponding Eulerian streaming patterns. The arrows in (d) and (e) are scaled logarithmically with the magnitude of the instantaneous first-order velocity, while they are normalized in (f) and (g). [(d), (f)] $\delta/a = 0.2$; [(e), (g)] $\delta/a = 5$. [(h), (i)] 3D views of the axisymmetric “half” geometry with $L = \tilde{a}$.

ARF, for a particle of radius a that is comparable to or smaller than the viscous boundary layer thickness δ . On a range of materials spanning from polystyrene to gold, in water, we showed that the ARF for $\delta/a > 1$ is generally dominated by the microstreaming contribution to the ARF, except for the nearly neutrally buoyant particles (e.g., polystyrene). Furthermore, we found that at $\delta/a \approx 1$, the viscous scattering contribution can be larger than the microstreaming contribution to the ARF, and that the greater density of the particle surprisingly shifts the rise of the microstreaming contribution towards higher δ/a .

Our analysis suggests that when the particle is comparable or smaller than δ , using simplified first-order models that neglect the microstreaming, such as the model by Settles and Bruus [42], can lead to substantial quantitative and qualitative errors. Instead, we propose to use a relatively simple analyti-

cal model that combines the density-related viscous scattering and microstreaming contributions to the ARF from Doinikov [22], and the compressibility-related inviscid scattering contribution from Yosioka and Kawasima [32]. The proposed hybrid model is in agreement with our numerical model for the studied range of particle materials and sizes.

Studying spheroids and spheres with protruding crowns revealed that the influence of shape on the ARF is insignificant for the particles with low density contrast to the surrounding fluid (e.g. polystyrene in Fig. 11), as is the case for biological cells. This could be relevant for the measurements of the acoustic compressibility of cells through the acoustic contrast factor [56], which can be used to assess, for example, the metastatic potential of a cell [76]. For denser particles, the influence of the spheroidal shape on the viscous contributions to the ARF is relatively insignificant. This happens in part

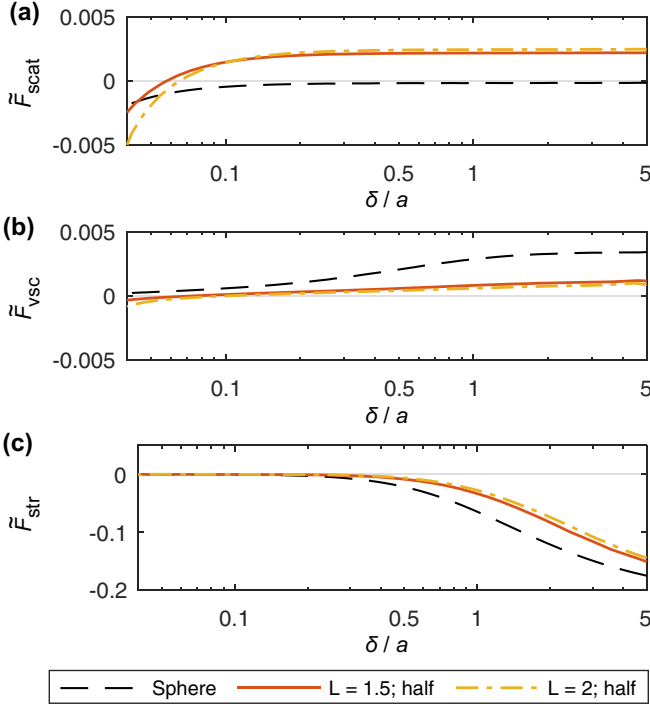


FIG. 11. Influence of a multicrown particle shape on the ARF and microstreaming with respect to the effective particle radius a . (a) The inviscid scattering contribution to the ARF due to the particle shape (\tilde{F}_{scat}), (b) the viscous scattering contribution to the ARF (\tilde{F}_{vsc}), and (c) the microstreaming contribution to the ARF (\tilde{F}_{str}). The polystyrene (PS) particle is in water, positioned in the middle between the pressure node and antinode of a standing wave with a frequency of 500 kHz, yielding $\delta = 0.74 \mu\text{m}$. The multicrown shape includes four crowns placed on the $z > 0$ hemisphere with a 20° step from the $z = 0$ plane (“half”); crown length L from the sphere surface is varied between $1.5\bar{a}$ and $2\bar{a}$, with \bar{a} defined as the radius of the base sphere on which the crowns are attached. The total volume of the multicrown particle is constrained to $V = 4\pi a^3/3$.

due to these contributions being negligible at $\delta/a < 1$, and in part due to the viscous boundary layer extending past the geometrical features that are $O(a)$ when the viscous contributions become relevant at $\delta/a > 1$. In contrast, the extreme shape perturbations in the form of sharp crowns can give rise to viscous ARF contributions at $\delta/a \ll 1$ (e.g., copper in Fig. 10).

In the future, the influence of the geometry on the viscous ARF contributions could be experimentally verified by tracking and comparing the motion of, for example, silver nanourchins [77] that resemble the shape of our multicrown model to the motion of spheres of equivalent volume in a standing wave. Furthermore, the ARF for cases investigated here could be experimentally measured directly, using an optical trap in combination with a standard bulk acoustic wave (BAW) device that can provide a quasi-one-dimensional standing acoustic wave, as demonstrated by Lamprecht *et al.* [78]. A study equivalent to Ref. [78] would not be feasible for a particle that satisfies the condition $\delta/a > 1$, since the drag on the particle from the environmental acoustic streaming in the BAW device would dominate the total measured force on the particle [24]. However, using an adjusted optical trap, Goering

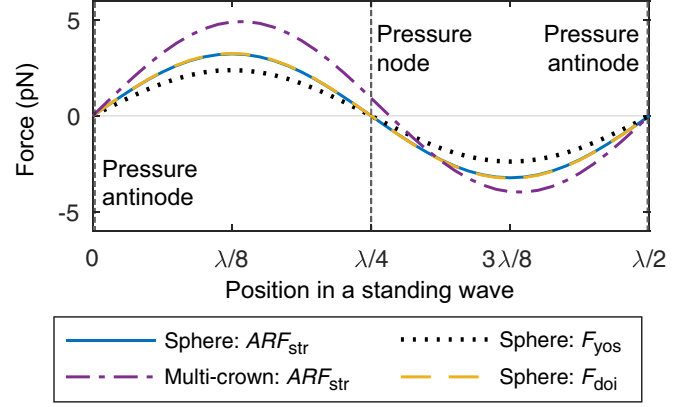


FIG. 12. Influence of the position of a copper (Cu) particle in a standing wave on the ARF, for $\delta/a = 0.5$. The particle is in water, with the position varied from one pressure antinode to another, passing through a pressure node, as indicated by the vertical dotted lines. The wave has an amplitude of 500 kPascal and a frequency of 500 kHz, yielding $\delta = 0.74 \mu\text{m}$. The multicrown shape includes four crowns placed on the $z > 0$ hemisphere with a 20° step from the $z = 0$ plane (“half”); crown length L from the sphere surface is equal to \bar{a} , with \bar{a} defined as the radius of the base sphere on which the crowns are attached. The total volume of the multicrown particle is constrained to $V = 4\pi a^3/3$. For a reference, the ARF on an equivalent sphere is computed with our viscous numerical model (ARF_{str}), with the inviscid model (F_{yos}) by Yosioka and Kawasima [32], and with the viscous rigid-particle model (F_{doi}) by Doinikov [22].

and Dual [79,80], recently measured that the build-up time of the ARF in such a BAW device is significantly shorter than the build-up time of the environmental streaming. This would potentially allow for the measurement of the ARF in the time span prior to the build up of the environmental streaming, consequently minimizing the influence of the environmental streaming on the measured force. This would be possible under the assumption that the microstreaming and the scattering contributions to the ARF on the particle would both build up significantly faster than the environmental streaming.

To bring the theoretical analysis closer to the experimental configuration, the numerical model could be extended to account for thermal effects. The effect of walls in experimental devices on the inviscid ARF is understood to be mostly negligible, except for some fluid-particle material combinations in close proximity to the walls [81]. However, in the case of the ARF that is dominated by the viscous contributions, the interaction between the walls and the particle could be much more significant, as indicated by the recent study on the microstreaming-inclusive acoustic interactions between two particles in a standing wave [59]. The wall effects could be studied in the future, by adding the wall domain to the model, and expanding the computational domain along the z axis.

The findings of our study bear the most significance for the acoustic manipulation of particles that are smaller than δ . The manipulation of such particles is very challenging in regular acoustofluidic devices due to the prevailing influence of the acoustic streaming at the scale of the fluidic cavity [24,82]. However, the continuous efforts towards the suppression of

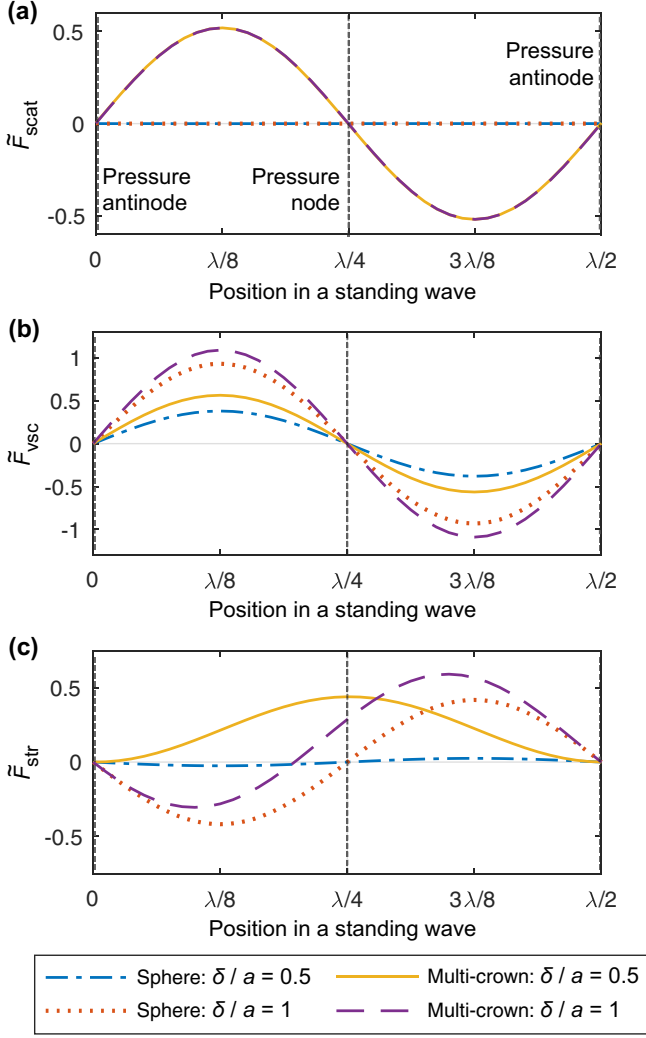


FIG. 13. Influence of the position of a copper (Cu) particle in a standing wave on the relative contributions to the ARF. (a) The inviscid scattering contribution to the ARF due to the particle shape (\tilde{F}_{scat}), (b) the viscous scattering contribution to the ARF (\tilde{F}_{vsc}), and (c) the microstreaming contribution to the ARF (\tilde{F}_{str}). The particle is in water, with the position varied from one pressure antinode to another, passing through a pressure node, as indicated by the vertical dotted lines. The wave has a frequency of 500 kHz, yielding $\delta = 0.74 \mu\text{m}$. The multicrown shape includes four crowns placed on the $z > 0$ hemisphere with a 20° step from the $z = 0$ plane (“half”); crown length L from the sphere surface is equal to \tilde{a} , with \tilde{a} defined as the radius of the base sphere on which the crowns are attached. The total volume of the multicrown particle is constrained to $V = 4\pi a^3/3$.

the latter [25,26,30,83] will inevitably open the door to the manipulation of particles smaller than δ .

APPENDIX A: INFLUENCE OF THE ROTATIONAL FIRST-ORDER VELOCITY FIELD

The simplified expression for the ARF from Eq. (18), introduced by Settnes and Bruus [42], neglects the microstreaming, while accounting for the viscous scattering effects at the first order. This is made possible through the arbitrary integration surface S_0 enclosing the particle in Eq. (15) that allows for

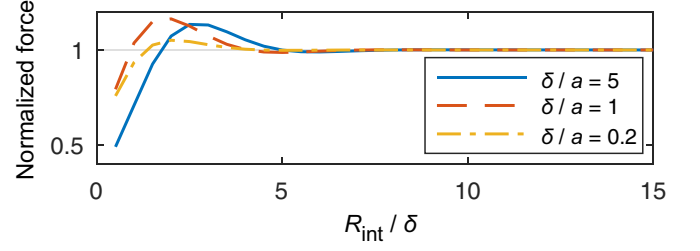


FIG. 14. Influence of the distance R_{int} of the spherical integration surface S_0 from the particle surface (radius a) on the first-order viscous ARF ($F_{\text{rad}}^{\text{noStr}}$) that neglects the microstreaming and the rotational first-order velocity field. The force $F_{\text{rad}}^{\text{noStr}} \cdot e_z$ is normalized by the force at $R_{\text{int}} = 15\delta$, for the respective particle radii $a = 5\delta$, $a = 1\delta$, and $a = 0.2\delta$. The gold (Au) particle is in water, positioned in the middle between the pressure node and antinode of a standing wave with an amplitude of 500 kPa and a frequency of 500 kHz, yielding $\delta = 0.74 \mu\text{m}$.

integration over the irrotational velocity field in the bulk of the fluid, away from the rotational viscous boundary layer δ that develops around the particle. In Fig. 14 we analyze the distance from the particle at which the simplified first-order viscous ARF neglecting the microstreaming ($F_{\text{rad}}^{\text{noStr}}$) becomes independent of the integration surface. This distance, at $\sim 5\delta$, appears to be consistent with the predictions in the literature [42].

APPENDIX B: DOINIKOV'S ANALYTICAL ARF MODEL ACCOUNTING FOR MICROSTREAMING AROUND AN INCOMPRESSIBLE PARTICLE

Here we describe F_{doi} that stems from Eqs. (5.15) and (6.1)–(6.8) of Ref. [22] and is valid for the acoustic radiation force on an incompressible spherical particle (radius a) in a viscous fluid in the Rayleigh limit ($ka \ll 1$), with no restriction on δ/a . The ARF along the direction of the pressure gradient of the standing wave follows as

$$F_{\text{doi}} = \frac{3}{4}\pi\rho_0\varphi_a\varphi_a^* \sum_{n=0}^1 (-1)^n (n+1) \times (D_n \sin 2kh + D_n^* \sin 2k^*h), \quad (\text{B1})$$

with the distance between the center of the particle and the nearest velocity node h . The coefficients D_0 and D_1 are computed as

$$D_0 = \frac{2x^3}{9} + \frac{x^3}{3x_V^3} - x^3 G_0(x_V, \lambda_\rho) [G_1(x_V) + x_V^3 (12 + x_V^2) f(x_V)], \quad (\text{B2})$$

$$D_1 = \frac{x^3}{3x_V^2} + \frac{x^3 G_0^*(x_V, \lambda_\rho)}{1 + x_V} \{G_2(x_V) - x_V^3 [2G_3(x_V) f(x_V) + iG_4(x_V) f(-ix_V) - 2(1+i)(9 + x_V^2) f(x_V - ix_V)]\}, \quad (\text{B3})$$

with

$$G_0(x_V, \lambda_\rho) = (1 - \lambda_\rho) \{72[9\lambda_\rho + 9\lambda_\rho x_V + (2 + \lambda_\rho)x_V^2]\}^{-1}, \quad (\text{B4})$$

$$G_1(x_V) = 48 - 96x_V + 2x_V^2 - 14x_V^3 + x_V^4 - x_V^5, \quad (\text{B5})$$

$$\begin{aligned} G_2(x_V) = & 48 + (48 + 192i/5)x_V \\ & + (122 + 192i)x_V^2/5 + 42(1 - i)x_V^3/5 \\ & + (49 + 36i)x_V^4/10 - (31 - 17i)x_V^5/10 \\ & + (6 + 31i)x_V^6/30 + (1 + 6i)x_V^7/30 + ix_V^8/30, \end{aligned} \quad (\text{B6})$$

$$G_3(x_V) = 3 - 3ix_V - x_V^2, \quad (\text{B7})$$

$$G_4(x_V) = 9 + 9x_V + 41x_V^2/10 + 11x_V^3/10 + x_V^4/5 + x_V^5/30, \quad (\text{B8})$$

$$f(z) = ze^z E_1(z), \quad (\text{B9})$$

where $E_1(z)$ is the integral exponent of the first order [84], $\lambda_\rho = \rho_0/\rho_p$ is the density ratio, and $x_V = a(1 + i)/\delta$.

-
- [1] S. O. Mast, Structure, movement, locomotion, and stimulation in amoeba, *J. Morphol.* **41**, 347 (1926).
- [2] K. D. Young, Bacterial morphology: Why have different shapes?, *Curr. Opin. Microbiol.* **10**, 596 (2007).
- [3] Y. Wang, Z. J. Han, S. F. Yu, R. R. Song, H. H. Song, K. K. Ostrikov, and H. Y. Yang, Core-leaf onion-like carbon/MnO₂ hybrid nano-urchins for rechargeable lithium-ion batteries, *Carbon* **64**, 230 (2013).
- [4] B. Angelov and I. M. Mladenov, On the geometry of red blood cell, in *Proceedings of the International Conference on Geometry, Integrability and Quantization*, Institute of Biophysics (Bulgarian Academy of Sciences, Acad. G. Bonchev Street, Sofia, Bulgaria, 2000), p. 27.
- [5] T. Laurell, F. Petersson, and A. Nilsson, Chip integrated strategies for acoustic separation and manipulation of cells and particles, *Chem. Soc. Rev.* **36**, 492 (2007).
- [6] M. Evander and J. Nilsson, Acoustofluidics 20: Applications in acoustic trapping, *Lab Chip* **12**, 4667 (2012).
- [7] M. E. Piyasena, P. P. Austin Suthanthiraraj, R. W. Applegate Jr, A. M. Goumas, T. A. Woods, G. P. López, and S. W. Graves, Multinode acoustic focusing for parallel flow cytometry, *Anal. Chem.* **84**, 1831 (2012).
- [8] F. B. Wijaya and K.-M. Lim, Numerical calculation of acoustic radiation force and torque acting on rigid non-spherical particles, *Acta Acust. Acust.* **101**, 531 (2015).
- [9] J. Wang and J. Dual, Theoretical and numerical calculations for the time-averaged acoustic force and torque acting on a rigid cylinder of arbitrary size in a low viscosity fluid, *J. Acoust. Soc. Am.* **129**, 3490 (2011).
- [10] J. Wang and J. Dual, Theoretical and numerical calculation of the acoustic radiation force acting on a circular rigid cylinder near a flat wall in a standing wave excitation in an ideal fluid, *Ultrasonics* **52**, 325 (2012).
- [11] G. T. Silva and B. W. Drinkwater, Acoustic radiation force exerted on a small spheroidal rigid particle by a beam of arbitrary wavefront: Examples of traveling and standing plane waves, *J. Acoust. Soc. Am.* **144**, EL453 (2018).
- [12] J. P. Leao-Neto, M. Hoyos, J.-L. Aider, and G. T. Silva, Acoustic radiation force and torque on spheroidal particles in an ideal cylindrical chamber, *J. Acoust. Soc. Am.* **149**, 285 (2021).
- [13] P. Hahn, I. Leibacher, T. Baasch, and J. Dual, Numerical simulation of acoustofluidic manipulation by radiation forces and acoustic streaming for complex particles, *Lab Chip* **15**, 4302 (2015).
- [14] Z. Gong, P. L. Marston, and W. Li, T-matrix evaluation of three-dimensional acoustic radiation forces on nonspherical objects in Bessel beams with arbitrary order and location, *Phys. Rev. E* **99**, 063004 (2019).
- [15] E. B. Lima and G. T. Silva, Mean acoustic fields exerted on a subwavelength axisymmetric particle, *J. Acoust. Soc. Am.* **150**, 376 (2021).
- [16] H. Bruus, Acoustofluidics 7: The acoustic radiation force on small particles, *Lab Chip* **12**, 1014 (2012).
- [17] Lord Rayleigh, On the circulation of air observed in Kundt's tubes, and on some allied acoustical problems, *Philos. Trans. R. Soc. London* **175**, 1 (1884).
- [18] H. Schlichting, Berechnung ebener periodischer Grenzschichtströmungen, *Phys. Z.* **33**, 327 (1932).
- [19] C. Eckart, Vortices and streams caused by sound waves, *Phys. Rev.* **73**, 68 (1948).
- [20] A. Lenshof, C. Magnusson, and T. Laurell, Acoustofluidics 8: Applications of acoustophoresis in continuous flow microsystems, *Lab Chip* **12**, 1210 (2012).
- [21] W. Nyborg, Ultrasonic microstreaming and related phenomena, *Brit. J. Cancer Suppl.* **5**, 156 (1982).
- [22] A. Doinikov, Acoustic radiation pressure on a rigid sphere in a viscous fluid, *Proc. R. Soc. London A* **447**, 447 (1994).
- [23] A. Rednikov and N. Riley, A simulation of streaming flows associated with acoustic levitators, *Phys. Fluids* **14**, 1502 (2002).
- [24] R. Barnkob, P. Augustsson, T. Laurell, and H. Bruus, Acoustic radiation-and streaming-induced microparticle velocities determined by microparticle image velocimetry in an ultrasound symmetry plane, *Phys. Rev. E* **86**, 056307 (2012).
- [25] J. S. Bach and H. Bruus, Suppression of Acoustic Streaming in Shape-Optimized Channels, *Phys. Rev. Lett.* **124**, 214501 (2020).
- [26] B. G. Winkelmann and H. Bruus, Theory and simulation of electroosmotic suppression of acoustic streaming, *J. Acoust. Soc. Am.* **149**, 3917 (2021).
- [27] P. B. Muller and H. Bruus, Theoretical study of time-dependent, ultrasound-induced acoustic streaming in microchannels, *Phys. Rev. E* **92**, 063018 (2015).
- [28] M. Hoyos and A. Castro, Controlling the acoustic streaming by pulsed ultrasounds, *Ultrasonics* **53**, 70 (2013).
- [29] A. Castro and M. Hoyos, Study of the onset of the acoustic streaming in parallel plate resonators with pulse ultrasound, *Ultrasonics* **66**, 166 (2016).
- [30] J. T. Karlsen, W. Qiu, P. Augustsson, and H. Bruus, Acoustic Streaming and Its Suppression in Inhomogeneous Fluids, *Phys. Rev. Lett.* **120**, 054501 (2018).
- [31] L. V. King, On the acoustic radiation pressure on spheres, *Proc. R. Soc. London A* **147**, 212 (1934).
- [32] K. Yosioka and Y. Kawasima, Acoustic radiation pressure on a compressible sphere, *Acta Acust. Acust.* **5**, 167 (1955).

- [33] L. P. Gor'kov, On the forces acting on a small particle in an acoustical field in an ideal fluid, *Sov. Phys. Dokl.* **6**, 773 (1962).
- [34] A. A. Doinikov, Acoustic radiation pressure on a compressible sphere in a viscous fluid, *J. Fluid Mech.* **267**, 1 (1994).
- [35] A. A. Doinikov, Acoustic radiation force on a spherical particle in a viscous heat-conducting fluid. I. General formula, *J. Acoust. Soc. Am.* **101**, 713 (1997).
- [36] A. A. Doinikov, Acoustic radiation force on a spherical particle in a viscous heat-conducting fluid. II. Force on a rigid sphere, *J. Acoust. Soc. Am.* **101**, 722 (1997).
- [37] A. A. Doinikov, Acoustic radiation force on a spherical particle in a viscous heat-conducting fluid. III. Force on a liquid drop, *J. Acoust. Soc. Am.* **101**, 731 (1997).
- [38] Z. Gong and M. Baudoin, Equivalence between angular spectrum-based and multipole expansion-based formulas of the acoustic radiation force and torque, *J. Acoust. Soc. Am.* **149**, 3469 (2021).
- [39] T. Baasch, A. Pavlic, and J. Dual, Acoustic radiation force acting on a heavy particle in a standing wave can be dominated by the acoustic microstreaming, *Phys. Rev. E* **100**, 061102(R) (2019).
- [40] A. Rednikov and S. S. Sadhal, Steady streaming from an oblate spheroid due to vibrations along its axis, *J. Fluid Mech.* **499**, 345 (2004).
- [41] A. Rednikov and S. S. Sadhal, Acoustic/steady streaming from a motionless boundary and related phenomena: Generalized treatment of the inner streaming and examples, *J. Fluid Mech.* **667**, 426 (2011).
- [42] M. Settnes and H. Bruus, Forces acting on a small particle in an acoustical field in a viscous fluid, *Phys. Rev. E* **85**, 016327 (2012).
- [43] See Supplemental Material at <http://link.aps.org/supplemental/10.1103/PhysRevE.106.015105>, which includes viscous and inviscid COMSOL models; Matlab functions for calculating F_{yos} , F_{sett} , F_{doi} , F_{hyb} ; Matlab scripts for running an exemplary numerical study with LiveLink for Matlab; and convergence studies related to the numerical model.
- [44] M. F. Hamilton, D. T. Blackstock *et al.*, *Nonlinear Acoustics*, Vol. 237 (Academic Press, San Diego, 1998).
- [45] J. T. Karlsen and H. Bruus, Forces acting on a small particle in an acoustical field in a thermoviscous fluid, *Phys. Rev. E* **92**, 043010 (2015).
- [46] D. T. Blackstock, *Fundamentals of Physical Acoustics* A Wiley-Interscience publication (John Wiley & Sons, New York, 2000).
- [47] J. Lighthill, Acoustic streaming, *J. Sound Vib.* **61**, 391 (1978).
- [48] T. Baasch, A. A. Doinikov, and J. Dual, Acoustic streaming outside and inside a fluid particle undergoing monopole and dipole oscillations, *Phys. Rev. E* **101**, 013108 (2020).
- [49] D. Andrews and M. McIntyre, An exact theory of nonlinear waves on a Lagrangian-mean flow, *J. Fluid Mech.* **89**, 609 (1978).
- [50] O. Bühler, *Waves and Mean Flows* (Cambridge University Press, 2014).
- [51] M. F. Hamilton, Y. A. Ilinskii, and E. A. Zabolotskaya, Acoustic streaming generated by standing waves in two-dimensional channels of arbitrary width, *J. Acoust. Soc. Am.* **113**, 153 (2003).
- [52] A. Pavlic and J. Dual, On the streaming in a microfluidic Kundt's tube, *J. Fluid Mech.* **911** (2021).
- [53] M. Wiklund, R. Green, and M. Ohlin, Acoustofluidics 14: Applications of acoustic streaming in microfluidic devices, *Lab Chip* **12**, 2438 (2012).
- [54] N. R. Skov, J. S. Bach, B. G. Winkelmann, and H. Bruus, 3D modeling of acoustofluidics in a liquid-filled cavity including streaming, viscous boundary layers, surrounding solids, and a piezoelectric transducer, *Aims Math.* **4**, 99 (2019).
- [55] A. R. Selfridge, Approximate material properties in isotropic materials, *IEEE Trans. Sonics Ultrason.* **32**, 381 (1985).
- [56] D. Hartono, Y. Liu, P. L. Tan, X. Y. S. Then, L.-Y. L. Yung, and K.-M. Lim, On-chip measurements of cell compressibility via acoustic radiation, *Lab Chip* **11**, 4072 (2011).
- [57] V. P. Jani, A. Lucas, V. P. Jani, C. Munoz, A. T. Williams, D. Ortiz, O. Yalcin, and P. Cabrales, Numerical model for the determination of erythrocyte mechanical properties and wall shear stress *in vivo* from intravital microscopy, *Front. Physiol.* **10**, 1562 (2020).
- [58] COMSOL Multiphysics v. 5.6, COMSOL AB, Stockholm, Sweden, 2020.
- [59] A. Pavlic, L. Ermanni, and J. Dual, Interparticle attraction along the direction of the pressure gradient in an acoustic standing wave, *Phys. Rev. E* **105**, L053101 (2022).
- [60] W. Ran and J. Saylor, The directional sensitivity of the acoustic radiation force to particle diameter, *J. Acoust. Soc. Am.* **137**, 3288 (2015).
- [61] C. Zhang, X. Guo, L. Royon, and P. Brunet, Unveiling of the mechanisms of acoustic streaming induced by sharp edges, *Phys. Rev. E* **102**, 043110 (2020).
- [62] A. Garbin, I. Leibacher, P. Hahn, H. Le Ferrand, A. Studart, and J. Dual, Acoustophoresis of disk-shaped microparticles: A numerical and experimental study of acoustic radiation forces and torques, *J. Acoust. Soc. Am.* **138**, 2759 (2015).
- [63] M. Ovchinnikov, J. Zhou, and S. Yalamanchili, Acoustic streaming of a sharp edge, *J. Acoust. Soc. Am.* **136**, 22 (2014).
- [64] N. Nama, P.-H. Huang, T. J. Huang, and F. Costanzo, Investigation of acoustic streaming patterns around oscillating sharp edges, *Lab Chip* **14**, 2824 (2014).
- [65] C. Zhang, X. Guo, L. Royon, and P. Brunet, Acoustic streaming generated by sharp edges: The coupled influences of liquid viscosity and acoustic frequency, *Micromachines* **11**, 607 (2020).
- [66] A. A. Doinikov, M. S. Gerlt, A. Pavlic, and J. Dual, Acoustic streaming produced by sharp-edge structures in microfluidic devices, *Microfluid. Nanofluid.* **24**, 32 (2020).
- [67] J. Hu, J. Yang, and J. Xu, Ultrasonic trapping of small particles by sharp edges vibrating in a flexural mode, *Appl. Phys. Lett.* **85**, 6042 (2004).
- [68] I. Leibacher, W. Dietze, P. Hahn, J. Wang, S. Schmitt, and J. Dual, Acoustophoresis of hollow and core-shell particles in two-dimensional resonance modes, *Microfluid. Nanofluid.* **16**, 513 (2014).
- [69] A. A. Doinikov, M. S. Gerlt, and J. Dual, Acoustic Radiation Forces Produced by Sharp-Edge Structures in Microfluidic Systems, *Phys. Rev. Lett.* **124**, 154501 (2020).
- [70] N. Nama, P.-H. Huang, T. J. Huang, and F. Costanzo, Investigation of micromixing by acoustically oscillated sharp-edges, *Biomicrofluidics* **10**, 024124 (2016).
- [71] C. Zhang, X. Guo, P. Brunet, M. Costalonga, and L. Royon, Acoustic streaming near a sharp structure and its mixing performance characterization, *Microfluid. Nanofluid.* **23**, 104 (2019).

- [72] P.-H. Huang, N. Nama, Z. Mao, P. Li, J. Rufo, Y. Chen, Y. Xie, C.-H. Wei, L. Wang, and T. J. Huang, A reliable and programmable acoustofluidic pump powered by oscillating sharp-edge structures, *Lab Chip* **14**, 4319 (2014).
- [73] A. Pavlic, C. L. Harshbarger, L. Rosenthaler, J. G. Snedeker, and J. Dual, Sharp-edge-based acoustofluidic chip for programmable pumping, mixing, cell focusing and trapping (unpublished).
- [74] F. Nadal and E. Lauga, Asymmetric steady streaming as a mechanism for acoustic propulsion of rigid bodies, *Phys. Fluids* **26**, 082001 (2014).
- [75] M. Kaynak, A. Ozcelik, A. Nourhani, P. E. Lammert, V. H. Crespi, and T. J. Huang, Acoustic actuation of bioinspired microswimmers, *Lab Chip* **17**, 395 (2017).
- [76] H. Wang, Z. Liu, D. M. Shin, Z. G. Chen, Y. Cho, Y.-J. Kim, and A. Han, Single-cell compressibility quantification for assessing metastatic potential of cancer cells through multi-frequency acoustophoresis, *Microfluid. Nanofluid.* **22**, 68 (2018).
- [77] S. D'Agostino and F. Della Sala, Silver nanourchins in plasmonics: Theoretical investigation on the optical properties of the branches, *J. Phys. Chem. C* **115**, 11934 (2011).
- [78] A. Lamprecht, S. Lakämper, T. Baasch, I. A. Schaap, and J. Dual, Imaging the position-dependent 3D force on microbeads subjected to acoustic radiation forces and streaming, *Lab Chip* **16**, 2682 (2016).
- [79] C. Goering and J. Dual, Dynamic measurement of the acoustic streaming time constant utilizing an optical tweezer, *Phys. Rev. E* **104**, 025104 (2021).
- [80] C. Goering and J. Dual, Measuring the effects of a pulsed excitation on the buildup of acoustic streaming and the acoustic radiation force utilizing an optical tweezer, *Phys. Rev. E* **105**, 055103 (2022).
- [81] T. Baasch and J. Dual, Acoustic Radiation Force on a Spherical Fluid or Solid Elastic Particle Placed Close to a Fluid or Solid Elastic Half-Space, *Phys. Rev. Appl.* **14**, 024052 (2020).
- [82] W. Qiu, H. Bruus, and P. Augustsson, Particle-size-dependent acoustophoretic motion and depletion of micro- and nanoparticles at long timescales, *Phys. Rev. E* **102**, 013108 (2020).
- [83] W. Qiu, J. T. Karlsen, H. Bruus, and P. Augustsson, Experimental Characterization of Acoustic Streaming in Gradients of Density and Compressibility, *Phys. Rev. Appl.* **11**, 024018 (2019).
- [84] M. Abramowitz and I. A. Stegun, *Handbook of Mathematical Functions: With Formulas, Graphs, and Mathematical Tables*, Dover Books on Intermediate and Advanced Mathematics Vol. 55 (Dover, New York, 1968).